CONDENSED MATTER PHYSICS

Single-electron spin resonance in a nanoelectronic device using a global field

Ensar Vahapoglu*[†], James P. Slack-Smith*[†], Ross C. C. Leon, Wee Han Lim, Fay E. Hudson, Tom Day, Tuomo Tanttu, Chih Hwan Yang, Arne Laucht, Andrew S. Dzurak*[‡], Jarryd J. Pla*[‡]

Spin-based silicon quantum electronic circuits offer a scalable platform for quantum computation, combining the manufacturability of semiconductor devices with the long coherence times afforded by spins in silicon. Advancing from current few-qubit devices to silicon quantum processors with upward of a million qubits, as required for fault-tolerant operation, presents several unique challenges, one of the most demanding being the ability to deliver microwave signals for large-scale qubit control. Here, we demonstrate a potential solution to this problem by using a three-dimensional dielectric resonator to broadcast a global microwave signal across a quantum nanoelectronic circuit. Critically, this technique uses only a single microwave source and is capable of delivering control signals to millions of qubits simultaneously. We show that the global field can be used to perform spin resonance of single electrons confined in a silicon double quantum dot device, establishing the feasibility of this approach for scalable spin qubit control.

INTRODUCTION

The ability to engineer quantum systems is expected to enable a range of transformational technologies including quantum-secured communication networks, enhanced sensors, and quantum computers, with applications spanning a diverse range of industries. Quantum computers are poised to significantly outperform their classical counterparts in many important problems such as quantum simulation (aiding materials and drug development) and optimization. While some applications are expected to be executable on medium-scale quantum computers (with 100 to 1000 qubits) that do not use error correction protocols (1), arguably the most disruptive algorithms (2) will require a large-scale and fully fault-tolerant quantum computer with upward of a million qubits (3, 4).

Of the possible physical implementations of qubits, electron spins in gate-defined silicon quantum dots (QDs) stand out for their long coherence times (5), their ability to operate at temperatures above 1 K (6, 7), and the potential to leverage the experience of the semiconductor industry in fabricating devices at scale. The building blocks for a spin-based quantum computer in silicon, namely, high-fidelity single (5) and two (8–10) qubit gates, have been demonstrated, and attention is now being directed toward the engineering challenges of constructing a large-scale processor (11). To achieve this ambitious goal, significant hurdles associated with qubit measurement and control must be overcome, such as how to deliver the microwave control signals to many qubits simultaneously, without disturbing the fragile cryogenic environment in which the processor operates.

One approach for spin qubit control successfully deployed in current few-qubit devices is based on a direct magnetic drive using an on-chip transmission line (12). A strong microwave current is passed through a wire placed close to the QD to generate an alternating magnetic field. Localization of the control field to the wire

demands a number of transmission lines that scales with the total number of qubits (13), while multiple high-frequency coaxial lines would be needed to deliver the control signals into the cryogenic system. The large microwave currents running through the processor in such a scheme raises concerns of heating, while the control lines themselves take up valuable chip real estate.

Electric dipole spin resonance (EDSR) (6, 14–18) is an alternative method for producing local spin control. For electron spin qubits, this technique simulates a magnetic drive by exploiting magnetic field gradients produced by nanomagnets in conjunction with microwave electric fields applied directly to the qubit gate electrodes. Integration of EDSR in large two-dimensional (2D) qubit arrays poses several challenges. In addition to the required transversal gradients, stray longitudinal gradients from the nanomagnets can cause spin decoherence. Furthermore, as with the transmission line–based direct magnetic drive, this technique requires microwave signals to be applied across many control lines, with multiple coaxial cables entering the system and both cross-talk and layout issues to overcome.

An elegant and potentially scalable spin qubit control solution was anticipated in the 1998 Kane proposal for a silicon quantum computer (19). In this approach, a single uniform global magnetic field is radiated across the entire processor (see Fig. 1A) (20, 21). Qubit operations are realized by applying potentials locally to spins to bring them in and out of resonance with the global field (22). This method uses a single microwave source and does not require the direct passage of strong high-frequency currents through the processor, reducing heating and simplifying the chip layout design.

Conventional electron spin resonance (ESR) spectroscopy (23) already provides a way to deliver global microwave fields to large ensembles of spins. The first-order approach to implementing global control for spin qubits in a quantum processor would be to simply place the chip inside a conventional 3D microwave cavity. However, internal device structures (such as metal gates and bond wires) adversely affect the properties of these microwave resonators (24). Furthermore, the chip is exposed to large alternating electric fields in these cavities. Such fields can interfere with (or potentially damage) the sensitive nanoelectronic devices used for qubit readout, cause photon-assisted tunneling (25), and increase heating of the device.
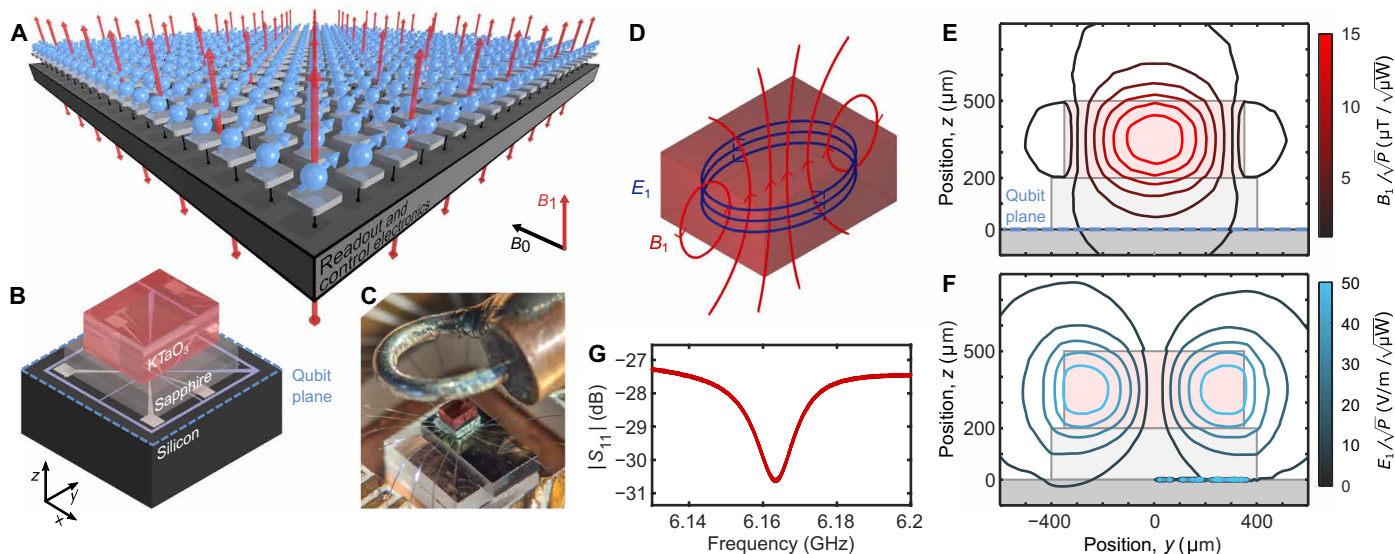
Fig. 1. Device stack for off-chip ESR and DR simulations. (**A**) A 3D render of the vision for large-scale qubit control using a global microwave field. (**B**) 3D graphic of the global control device stack as used in our experiments, including silicon quantum nanoelectronic device (bottom), sapphire dielectric spacer (middle), and potassium tantalate (KTaO$_3$) dielectric microwave resonator (top). The DR is a $0.7 \times 0.55 \times 0.3$ mm^3 rectangular prism. (**C**) A photograph of the device and coaxial loop coupler. Photo credit: James Slack Smith, School of Electrical Engineering and Telecommunications, UNSW Sydney. (**D**) Schematic depicting directions of the magnetic and electric field components of the TE$_{11\delta}$ mode in the DR. (**E** and **F**) Finite-element simulation of the conversion factors for the magnetic field z-component magnitude (E) and electric field magnitude (F) of the TE$_{11\delta}$ mode supported by the DR. P represents the microwave power input to the loop coupler. (**G**) S_{11} reflection parameter measurement near the fundamental mode of the DR, measured via the coaxial loop coupler.

An important metric for a microwave cavity is the power-to-field conversion factor C, which quantifies how well a microwave input signal is converted to the alternating magnetic field needed to drive spin rotations. The expression $B_1 = C\sqrt{P}$ relates the magnetic drive B_1 to the input signal power P through the conversion factor $C \propto \sqrt{Q/\omega V}$, which itself depends on the quality factor Q of the cavity, its frequency ω, and the microwave mode volume V. For low conversion factors (as obtained with conventional metallic cavity resonators), substantial powers are required to drive sufficiently fast spin rotations, powers potentially incompatible with the cryogenic environment of the quantum processor. To raise the conversion efficiency and reduce the driving power, cavities with high Q and small mode volumes are desirable.

While attempts have been made to control spins in nanoelectronic devices using 3D metallic ESR resonators (26), performing spin resonance with a global field has, until now, remained elusive. Here, we demonstrate ESR of single spins in a silicon metal oxide semiconductor (SiMOS) QD device by using a compact dielectric resonator (DR) placed above the chip (Fig. 1B). The DR is constructed from potassium tantalate (KTaO$_3$ or KTO), a quantum paraelectric material that exhibits an exceptionally high dielectric constant at cryogenic temperatures and, hence, compact microwave mode volumes. ESR control is confirmed to be resonator-driven by observing an enhancement in the mixing of the QD spin states within the DR bandwidth. This represents the first step toward the vision (see Fig. 1A) of large-scale qubit control using global magnetic fields generated off-chip.

RESULTS
DR and chip assembly
To overcome the challenges presented by global control, we desire a microwave cavity that minimizes the mode volume (while maximizing

surface area), maintains a large quality factor, and produces very little electric field at the chip. Here, we exploit a species of ESR cavity called a DR, a volume of dielectric material where the sudden transition between the high dielectric constant inside the material and the low dielectric constant outside it (vacuum) leads to the formation of standing waves. DRs are often used in conventional ESR spectroscopy (27) because of their high magnetic field–to–power conversion factors (C) and low intrinsic losses. Our DR is designed to operate in the TE$_{11\delta}$ mode (28), shown in Fig. 1D. In this mode, the DR acts like a magnetic dipole (i.e., a current loop). The magnetic field is strongest along the central axis (see Fig. 1E) and extends outside the DR, while the electric field is concentrated toward the outer edges and strongly confined inside the material (Fig. 1F).

The frequency of a DR is inversely proportional to the dielectric constant ε_r and its mode volume V, specifically $\omega \propto 1/(\sqrt{\varepsilon_r} \, V^{1/3})$. Thus, for a given frequency, the mode volume can be reduced by increasing ε_r. In this work, we exploit the perovskite material potassium tantalate. KTO is a quantum paraelectric, a material that displays ferroelectric-like properties (such as a high dielectric constant) but whose transition to the ferroelectric phase is suppressed by quantum fluctuations (29). KTO has an extraordinarily large dielectric constant at cryogenic temperatures ($\varepsilon_r \approx 4300$ for $T < 10$ K) and exhibits very low microwave losses (tan $\delta \sim 10^{-4}$ to 10^{-5}), permitting high internal quality factors (30).

The DR is cut in the shape of a rectangular prism and integrated with the silicon QD device as depicted in Fig. 1 (B and C). The smallest dimension of the prism is its height, as this allows us to increase the surface area over which the B_1 field is generated for a given DR volume (and, consequently, frequency). Our finite-element simulations indicate that B_1 has a good uniformity across the qubit plane, varying by less than 15% over a 0.2×0.2 mm^2 area (see the Supplementary Materials). We note, however, that this uniformity is

far from optimized and can readily be improved through adjustments to the DR dimensions. For example, working at lower microwave frequencies would allow the DR surface area to be increased and thus improve the lateral B_1 homogeneity. To minimize any stray electric fields reaching the device, a 200-μm-thick sapphire spacer [$\epsilon_R \approx 9.26$, tan (δ) $\approx 7 \times 10^{-7}$ (31)] is placed between the DR and silicon chip. The spacer also serves to distance the DR from any undesirable loss mechanisms in the chip and thus maximize the resonator Q and conversion factor. The B_1 field used for driving spin rotations is oriented perpendicular to the qubit plane when operating in the $TE_{11\delta}$ mode. The chip containing the silicon double quantum dot (DQD) device is wire-bonded to a printed circuit board and housed inside a copper enclosure to shield the sample and to suppress radiation losses from the DR. Microwave power is inductively coupled into the resonator through a coaxial cable terminated in a shorted loop (see Fig. 1C). The coupling strength of the DR to the coaxial port is determined primarily by the overlap between the DR and loop magnetic fields and can be controlled ex situ by altering the position of the loop.

Experiments are performed in a dilution refrigerator at a base temperature of 50 mK. We probe the frequency response of the resonator via an S_{11} measurement through the coaxial coupler (Fig. 1G) and extract a resonant frequency of the fundamental $TE_{11\delta}$ mode of 6.163 GHz at 50 mK. We measured an internal quality factor of $Q_i \approx 60,000$ for the resonator in a separate cool-down without the chip, in line with the best reported values of the microwave loss tangent for KTO (30). In practice, we find the quality factor of the

resonator to be limited by losses in the device and extract an internal quality factor of $Q_i \approx 500$. We believe that these losses are primarily due to heavily doped regions in the chip that are used in the existing fabrication process (refer to the Supplementary Materials). Finite-element simulations of the complete device assembly are performed to reproduce the measured DR S_{11} (see the Supplementary Materials) and indicate an exceptionally large conversion factor $C \approx 3 \, \mu T/\sqrt{\mu W}$.

Nanoelectronic device and spin readout

The single spins in this work are provided by a ^{nat}SiMOS DQD device, electrostatically defined by a palladium (Pd) gate stack architecture (32). Figure 2A shows a scanning electron microscope image of a device nominally identical to the one measured. A cross section through the dot channel depicting the gate stack and conduction band profile is illustrated in Fig. 2B. Critically, instead of having a microwave transmission line (12) or a micromagnet (18) fabricated on-chip with the QDs, here, we incorporate the coaxial loop coupler and DR on top of the silicon device to drive spin resonance in a global field.

To populate an arbitrary integer number of electrons ($N1$, $N2$) in Dot 1 and Dot 2, we apply positive voltages to gates D1 and D2. The electrons are loaded from an electron reservoir induced at the Si/SiO$_2$ interface by applying a positive bias to D3, D4, and RG. By lowering the voltages on confinement gates CB1, CB2, and SETB, we ensure that electrons in the two QDs are confined to small spatial regions, as indicated in Fig. 2A. The barrier gates RB and
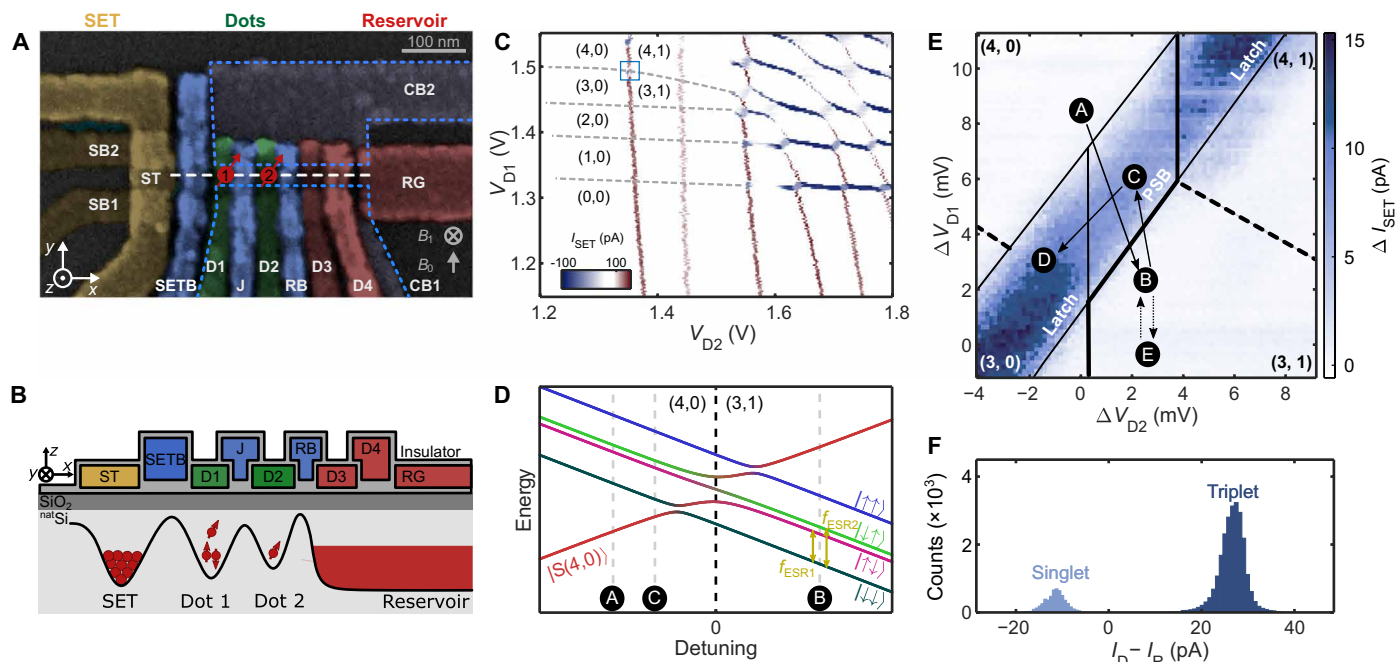
Fig. 2. Silicon double QD with latched Pauli spin blockade readout. (**A**) Scanning electron micrograph of the QD device with false coloring for the gate electrodes. (**B**) A schematic cross section through the middle of the device (indicated with a white dashed line in (A), showing the 3D structure of the gates and conduction band profile. (**C**) Charge stability diagram of the DQD obtained by monitoring the current I_{SET} through a nearby capacitively coupled charge sensor (a SET). The numbers in parentheses represent the charge occupancies of the double dot system Dot 1, Dot 2: ($N1$, $N2$). (**D**) Schematic energy diagram of the (4,0)-(3,1) anti-crossing. (**E**) Readout pulse sequence overlaid on a 2D color plot of the readout search signal ΔI_{SET} (see the Supplementary Materials for details) as a function of the voltages on gates D1 and D2. The absolute voltage range is indicated by the blue rectangle in (C). Readout is performed with the sequence B to D. The solid lines indicate transitions with high tunnel rates; the dashed lines indicate transitions with low tunnel rates, and the thin lines identify the PSB (Pauli spin blockade) and latched regions. (**F**) Histogram of the latched SET current signal for $|\downarrow\downarrow\rangle$ state initialization, indicating a $|\downarrow\downarrow\rangle$ initialization infidelity of 19%.

J allow us to control the tunnel coupling between the dots and the reservoir (RB) as well as the interdot coupling (J). A single-electron transistor (SET) nearby serves as a charge sensor to monitor the occupancy of the two QDs (5).

Figure 2C shows the charge stability diagram of the DQD system, measured via a double lock-in technique (33). The nearly horizontal lines (blue) correspond to charge transitions in Dot 1, while the nearly vertical lines (red) are caused by charge transitions in Dot 2. As we decrease V_{D1} and V_{D2} (the voltages applied to gates D1 and D2), electrons are depleted one by one from Dot 1 and Dot 2 until they are both completely empty, denoted as (0,0) in the lower left corner of the stability plot. The transitions of Dot 1 are not visible at lower V_{D2} because the tunnel rates between Dot 1 and the reservoir for these bias conditions are smaller than the lock-in probe frequency. These transitions are indicated with gray dashed lines as a visual aid. We note that the faint vertical transition visible at $V_{D2} \approx 1.45$ V is due to an unintentional dot formed under gate RB. The sensing signal is weaker owing to its distance from the SET sensor.

For the remainder of the paper, we focus on the (4,0)-(3,1) charge transition for singlet-triplet readout. Here, two of the electrons in Dot 1 form a spin-zero closed shell and do not interact with the third and fourth electrons during experiments. Spin readout is performed via the pulse sequence A to D indicated in Fig. 2E (see the Supplementary Materials for the experiment performed to obtain this 2D color map). Step A prepares the DQD system in the (4,0) singlet state. Then, by ramping adiabatically from A to B, the system is initialized in the triplet state $|\downarrow\downarrow\rangle$ (see the energy diagram in Fig. 2D). Pulsing from B to C attempts to move the electron from Dot 2 to Dot 1. If the electron in Dot 2 forms a singlet with the electron in Dot 1, tunneling takes place, producing a change in the charge configuration from (3,1) to (4,0). However, if a triplet state is formed, Pauli spin blockade (PSB) prevents the electron from tunneling and the system remains in the (3,1) charge configuration (34). The charge and, therefore, spin states can be differentiated by monitoring the SET current I_{SET}, a process referred to as spin-to-charge conversion. In addition, the sensitivity of the spin-to-charge conversion is enhanced using a latched PSB mechanism (32, 35) by pulsing quickly from C to D.

The histogram shown in Fig. 2F is formed by running 30,000 single-shot measurements and recording the difference of the SET current at pulse level D (I_D) and a reference level in the (4,0) region (I_R). The histogram reveals two peaks corresponding to measurements of singlet or triplet states. The singlet and triplet peaks are separated by 8.2σ, indicating a charge state readout infidelity on the order of 10^{-16}. Since the pulse sequence A to D ideally initializes and measures the system in the $|\downarrow\downarrow\rangle$ state, the appearance of the singlet histogram peak allows us to infer a $|\downarrow\downarrow\rangle$ initialization fidelity of 81%.

Single-electron spin resonance in a global field

Having demonstrated spin initialization and readout, we now investigate ESR in a global microwave magnetic field. Using the pulse sequence illustrated in Fig. 3A, we first initialize a $|\downarrow\downarrow\rangle$ state in the DQD system. We then apply microwave control pulses to the coaxial loop coupler, which excites the $TE_{11\delta}$ mode of the DR, generating a global alternating magnetic field, B_1, to manipulate the individual spins. When the DR frequency is resonant with either the $|\downarrow\downarrow\rangle \Leftrightarrow |\uparrow\downarrow\rangle$ or $|\downarrow\downarrow\rangle \Leftrightarrow |\downarrow\uparrow\rangle$ transitions (see Fig. 2D), which occurs at specific values of B_0, the spin states become mixed, reducing the probability of the system being in the $|\downarrow\downarrow\rangle$ state. The resonance

frequencies can be calculated with $f_{res} = g\mu_B B_0/h$, where g, μ_B, and h are the electron g-factor, Bohr magneton, and Planck constant, respectively. After spin manipulation, readout is performed by pulsing to the latched region (as described above) and classifying the detected
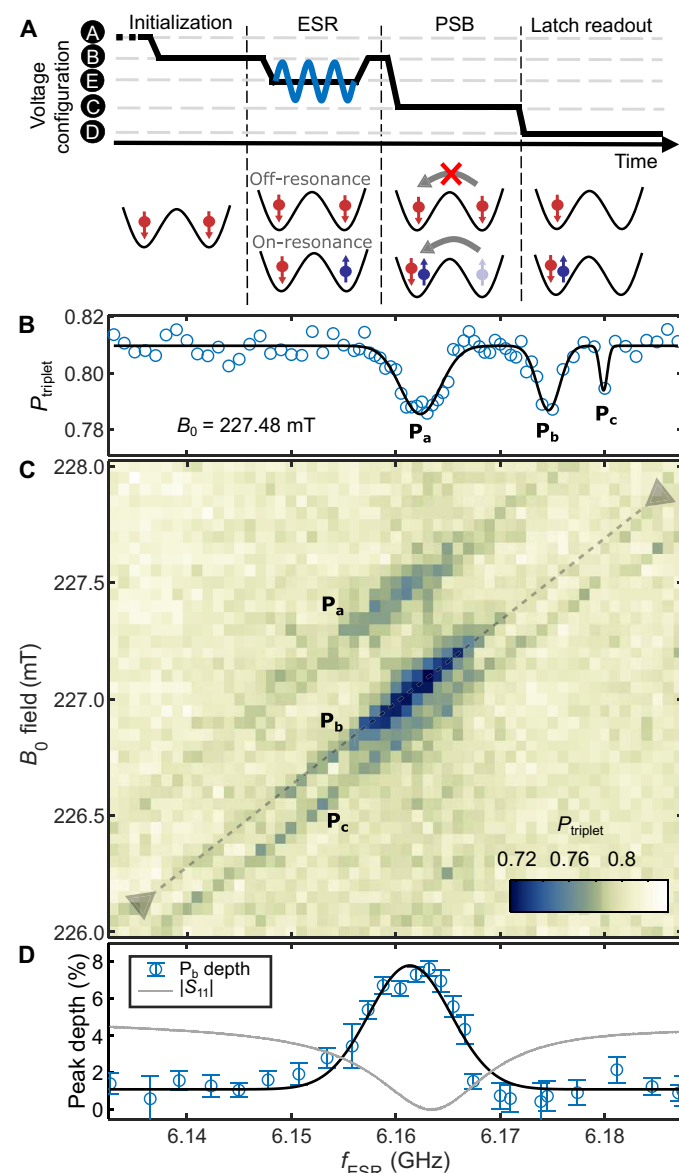
Fig. 3. ESR results. (**A**) Pulsing scheme for the ESR measurements. The DQD is initialized in a $|\downarrow\downarrow\rangle$ state. Microwave power is then applied to the DR, generating an alternating magnetic field, B_1, which can rotate the spins if they are in resonance with the field. Last, readout is performed to find the probability for the system to be in the triplet state. The cartoon below illustrates the spin states of the double dot system for each pulse stage, showing both the case when the ESR drive is on-resonance and when it is off-resonance. (**B**) Triplet probability as a function of the applied microwave frequency f_{ESR} at $B_0 = 227.48$ mT, showing three ESR peaks, two of which are consistent with the double dot system, while the third is an unexpected ESR peak. Note that (B) to (D) all share the same horizontal axis. (**C**) Triplet probability as a function of f_{ESR} and B_0, demonstrating that the ESR peaks shift with magnetic field, as expected. (**D**) Depth of the middle ESR peak (P_b) plotted as a function of the qubit frequency, demonstrating enhancement of the magnetic field inside the bandwidth of the DR. The resonator S_{11} is overlaid in gray (see Fig. 1G).

spin state as either triplet or singlet depending on the size of the recorded SET current. Repeating this sequence several times allows us to calculate the probability for measuring a $|\downarrow\downarrow\rangle$ state $P_{triplet}$. When the spins in either Dot 1 or Dot 2 are resonant with the DR, we measure a reduction in $P_{triplet}$. It is known that the electron g-factors can be different in each dot because of electric field–induced Stark shifts and device strains produced by thermal contraction of the metal gates (36, 37).

Figure 3B shows the ESR peaks driven by the DR as a function of applied microwave frequency at a static magnetic field B_0 = 227.48 mT. By fitting the experimental data (blue circles) to Gaussian distributions, we obtain two broad peaks P_a and P_b, with resonance frequencies of 6.163 GHz and 6.174 GHz, respectively, attributed to the DQD system, as well as a third peak P_c at 6.180 GHz, which could potentially result from an unintended spin state coupled to the DQD. To demonstrate that these peaks are spin-related, we measure the triplet probability as a function of B_0 and the B_1 drive frequency f_{ESR}, as shown in Fig. 3C. All three peaks exhibit a linear dependence on B_0, each having ≈54 MHz shift in a range of 2 mT B_0 field. The ESR frequencies are all consistent with electron spin g-factors in SiMOS QDs (37), which are generally slightly below g = 2, to an accuracy limited by the calibration of our DC superconducting magnet.

We observe that the visibility of the P_a and P_b signals is enhanced considerably when the microwave frequency f_{ESR} is within the bandwidth of the DR fundamental mode, as should be the case if ESR is being driven by a global field produced by the resonator. In Fig. 3D, we plot the ESR peak depth along the P_b transition as a function of ESR frequency, f_{ESR}, indicated by the dashed line in Fig. 3C and fit the result with a Lorentzian curve (black line). It is clear that the maximum peak depth coincides well with the S_{11} response of the DR (Fig. 1G; replotted with gray line in Fig. 3D for comparison). Outside the DR resonance bandwidth, the visibility of P_b saturates to approximately 1%, indicating that there is some residual drive that may, for example, originate from the coaxial loop coupler. However, the visibility is improved to 8% at the resonance frequency (6.163 GHz), demonstrating that the observed ESR is largely driven by the DR itself. For powers exceeding −32 dBm at the loop coupler, we observe transients in the measured SET current after application of the ESR pulse (see the Supplementary Materials), which coincides with the spin states being left in a fully mixed state. Consequently, we are not able to increase the microwave drive power beyond the ESR linewidth (Δf = 2 to 4 MHz) of the spins in this ^{nat}Si device, which is a prerequisite for observing Rabi oscillations.

DISCUSSION

A natural next step is the demonstration of coherent spin control. The measured device is fabricated on a ^{nat}Si substrate, which consists of approximately 4.7% ^{29}Si, having nonzero nuclear spins that cause significant inhomogeneous broadening of the resonance frequencies. Coherent spin driving therefore requires relatively fast Rabi frequencies, at least as large as the P_a and P_b transition linewidths of 4 MHz and 2 MHz, respectively (Fig. 3C). Moving to an isotopically enriched silicon substrate will substantially reduce the power requirements for observing coherent control (5).

The measured internal quality factor of the DR and device assembly is approximately two orders of magnitude lower than the

material limit for KTO ($Q_i \approx$ 60,000). Improvements in the quality factor could be made through device modifications to remove any microwave current loops and to minimize the overlap of the DR with lossy materials such as bond wires and the highly doped source and drain n$^+$ ohmic contacts. Reaching the material limit for Q would boost the conversion factor by an order of magnitude, decreasing the power requirements a hundredfold and allowing Rabi frequencies as large as 6 MHz for an input microwave power of just 200 µW. Device performance may also be improved by using a shielded loop coupler design (38), which would minimize any unwanted stray electric fields and associated device interference.

The successful demonstration of ESR in a nanoelectronic device using a global magnetic field, as reported here, is a crucial step on the path to scale-up of spin-based quantum processors. This work shows that 3D DRs can be integrated with nanoelectronic circuits and are a viable source of global magnetic fields. The high homogeneity area of the current DR (0.2 × 0.2 mm^2) would overlap with approximately 4 million qubits, assuming a conservative 100-nm qubit pitch (20). This area can be readily increased by reducing the height and/or frequency of the DR. We believe that with the proposed alterations to the chip design and resonator assembly, large-scale control of millions of spin qubits in a continuous microwave field is now a realistic prospect.

MATERIALS AND METHODS
Experimental setup
Our experiments were performed in a setup similar to previous work (5, 6), except for the delivery of the microwave signal to the device. The diagram in fig. S3 (see the Supplementary Materials) depicts how the signal generated by the microwave source is routed to the device. The signal reaches the coaxial loop coupler after going through a cryogenic circulator with a pass band of 4 to 8 GHz. The microwave signal produces an alternating current around the loop, generating a magnetic field that inductively couples to the DR field, as explained in the "DR and chip assembly" section. To measure the DR S_{11} response, we replace the microwave source with a vector network analyzer (VNA), where the reflected signal from the loop coupler is returned to the VNA via the circulator.

Background subtraction
The data in Fig. 3B and the 2D color map in Fig. 3C are postprocessed to remove background artifacts unrelated to the spins. A horizontal trace recorded at a B_0 far off resonance with spins is subtracted from the data. In addition, each horizontal trace is offset by its own median current to correct for any variation in the SET current level over time.

SUPPLEMENTARY MATERIALS
Supplementary material for this article is available at http://advances.sciencemag.org/cgi/content/full/7/33/eabg9158/DC1

REFERENCES AND NOTES
1. J. Preskill, Quantum computing in the NISQ era and beyond. *Quantum* **2**, 79 (2018).
2. P. W. Shor, in *Proceedings 35th Annual Symposium on Foundations of Computer Science* (IEEE, 1994), pp. 124–134.
3. A. G. Fowler, M. Mariantoni, J. M. Martinis, A. N. Cleland, Surface codes: Towards practical large-scale quantum computation. *Phys. Rev. A* **86**, 032324 (2012).
4. B. Lekitsch, S. Weidt, A. G. Fowler, K. Mølmer, S. J. Devitt, C. Wunderlich, W. K. Hensinger, Blueprint for a microwave trapped ion quantum computer. *Sci. Adv.* **3**, e1601540 (2017).

5. M. Veldhorst, J. C. C. Hwang, C. H. Yang, A. W. Leenstra, B. de Ronde, J. P. Dehollain, J. T. Muhonen, F. E. Hudson, K. M. Itoh, A. Morello, A. S. Dzurak, An addressable quantum dot qubit with fault-tolerant control-fidelity. *Nat. Nanotechnol.* **9**, 981–985 (2014).

6. C. H. Yang, R. C. C. Leon, J. C. C. Hwang, A. Saraiva, T. Tanttu, W. Huang, J. Camirand Lemyre, K. W. Chan, K. Y. Tan, F. E. Hudson, K. M. Itoh, A. Morello, M. Pioro-Ladrière, A. Laucht, A. S. Dzurak, Operation of a silicon quantum processor unit cell above one kelvin. *Nature* **580**, 350–354 (2020).

7. L. Petit, H. G. J. Eenink, M. Russ, W. I. L. Lawrie, N. W. Hendrickx, S. G. J. Philips, J. S. Clarke, L. M. K. Vandersypen, M. Veldhorst, Universal quantum logic in hot silicon qubits. *Nature* **580**, 355–359 (2020).

8. M. Veldhorst, C. H. Yang, J. C. C. Hwang, W. Huang, J. P. Dehollain, J. T. Muhonen, S. Simmons, A. Laucht, F. E. Hudson, K. M. Itoh, A. Morello, A. S. Dzurak, A two-qubit logic gate in silicon. *Nature* **526**, 410–414 (2015).

9. W. Huang, C. H. Yang, K. W. Chan, T. Tanttu, B. Hensen, R. C. C. Leon, M. A. Fogarty, J. C. C. Hwang, F. E. Hudson, K. M. Itoh, A. Morello, A. Laucht, A. S. Dzurak, Fidelity benchmarks for two-qubit gates in silicon. *Nature* **569**, 532–536 (2019).

10. X. Xue, T. F. Watson, J. Helsen, D. R. Ward, D. E. Savage, M. G. Lagally, S. N. Coppersmith, M. A. Eriksson, S. Wehner, L. M. K. Vandersypen, Benchmarking gate fidelities in a Si/SiGe two-qubit device. *Phys. Rev. X* **9**, 021011 (2019).

11. M. F. Gonzalez-Zalba, S. de Franceschi, E. Charbon, T. Meunier, M. Vinet, A. S. Dzurak, Scaling silicon-based quantum computing using CMOS technology: State-of-the-art, challenges and perspectives. arXiv:2011.11753 [quant-ph] (2020).

12. J. P. Dehollain, J. J. Pla, E. Siew, K. Y. Tan, A. S. Dzurak, A. Morello, Nanoscale broadband transmission lines for spin qubit control. *Nanotechnology* **24**, 015202 (2013).

13. R. Li, L. Petit, D. P. Franke, J. P. Dehollain, J. Helsen, M. Steudtner, N. K. Thomas, Z. R. Yoscovits, K. J. Singh, S. Wehner, L. M. K. Vandersypen, J. S. Clarke, M. Veldhorst, A crossbar network for silicon quantum dot qubits. *Sci. Adv.* **4**, eaar3960 (2018).

14. M. Pioro-Ladrière, T. Obata, Y. Tokura, Y.-S. Shin, T. Kubo, K. Yoshida, T. Taniyama, S. Tarucha, Electrically driven single-electron spin resonance in a slanting Zeeman field. *Nat. Phys.* **4**, 776–779 (2008).

15. E. Kawakami, P. Scarlino, D. R. Ward, F. R. Braakman, D. E. Savage, M. G. Lagally, M. Friesen, S. N. Coppersmith, M. A. Eriksson, L. M. K. Vandersypen, Electrical control of a long-lived spin qubit in a Si/SiGe quantum dot. *Nat. Nanotechnol.* **9**, 666–670 (2014).

16. K. Takeda, J. Kamioka, T. Otsuka, J. Yoneda, T. Nakajima, M. R. Delbecq, S. Amaha, G. Allison, T. Kodera, S. Oda, S. Tarucha, A fault-tolerant addressable spin qubit in a natural silicon quantum dot. *Sci. Adv.* **2**, e1600694 (2016).

17. T. Watson, S. G. J. Philips, E. Kawakami, D. R. Ward, P. Scarlino, M. Veldhorst, D. E. Savage, M. G. Lagally, M. Friesen, S. N. Coppersmith, M. A. Eriksson, L. M. K. Vandersypen, A programmable two-qubit quantum processor in silicon. *Nature* **555**, 633–637 (2018).

18. R. C. C. Leon, C. H. Yang, J. C. C. Hwang, J. C. Lemyre, T. Tanttu, W. Huang, K. W. Chan, K. Y. Tan, F. E. Hudson, K. M. Itoh, A. Morello, A. Laucht, M. Pioro-Ladrière, A. Saraiva, A. S. Dzurak, Coherent spin control of s-, p-, d- and f-electrons in a silicon quantum dot. *Nat. Commun.* **11**, 797 (2020).

19. B. E. Kane, A silicon-based nuclear spin quantum computer. *Nature* **393**, 133–137 (1998).

20. M. Veldhorst, H. G. J. Eenink, C. H. Yang, A. S. Dzurak, Silicon CMOS architecture for a spin-based quantum computer. *Nat. Commun.* **8**, 1766 (2017).

21. C. D. Hill, E. Peretz, S. J. Hile, M. G. House, M. Fuechsle, S. Rogge, M. Y. Simmons, L. C. L. Hollenberg, A surface code quantum computer in silicon. *Sci. Adv.* **1**, e1500707 (2015).

22. A. Laucht, J. T. Muhonen, F. A. Mohiyaddin, R. Kalra, J. P. Dehollain, S. Freer, F. E. Hudson, M. Veldhorst, R. Rahman, G. Klimeck, K. M. Itoh, D. N. Jamieson, J. C. McCallum, A. S. Dzurak, A. Morello, Electrically controlling single-spin qubits in a continuous microwave field. *Sci. Adv.* **1**, e1500022 (2015).

23. A. Schweiger, G. Jeschke, *Principles of Pulse Electron Paramagnetic Resonance* (Oxford Univ. Press on Demand, 2001).

24. W.-C. Kong, G.-W. Deng, S.-X. Li, H.-O. Li, G. Cao, M. Xiao, G.-P. Guo, Introduction of DC line structures into a superconducting microwave 3D cavity. *Rev. Sci. Instrum.* **86**, 023108 (2015).

25. L. P. Kouwenhoven, S. Jauhar, K. McCormick, D. Dixon, P. L. McEuen, Y. V. Nazarov, N. C. van der Vaart, C. T. Foxon, Photon-assisted tunneling through a quantum dot. *Phys. Rev. B* **50**, 2019 (1994).

26. B. Simovič, P. Studerus, S. Gustavsson, R. Leturcq, K. Ensslin, R. Schuhmann, J. Forrer, A. Schweiger, Design of Q-band loop-gap resonators at frequencies of 34–36 GHz for single electron spin spectroscopy in semiconductor nanostructures. *Rev. Sci. Instrum.* **77**, 064702 (2006).

27. A. Blank, E. Stavitski, H. Levanon, F. Gubaydullin, Transparent miniature dielectric resonator for electron paramagnetic resonance experiments. *Rev. Sci. Instrum.* **74**, 2853–2859 (2003).

28. I. Geifman, I. S. Golovina, Electromagnetic characterization of rectangular ferroelectric resonators. *J. Magn. Reson.* **174**, 292–300 (2005).

29. S. Gevorgian, in *Ferroelectrics in Microwave Devices, Circuits and Systems: Physics, Modeling, Fabrication and Measurements* (Springer, 2009), pp. 21–59.

30. R. G. Geyer, B. Riddle, J. Krupka, L. A. Boatner, Microwave dielectric properties of single-crystal quantum paraelectrics K Ta O$_3$ and Sr Ti O$_3$ at cryogenic temperatures. *J. Appl. Phys.* **97**, 104111 (2005).

31. J. Krupka, K. Derzakowski, M. Tobar, J. Hartnett, R. G. Geyer, Complex permittivity of some ultralow loss dielectric crystals at cryogenic temperatures. *Meas. Sci. Technol.* **10**, 387–392 (1999).

32. R. Zhao, T. Tanttu, K. Y. Tan, B. Hensen, K. W. Chan, J. C. C. Hwang, R. C. C. Leon, C. H. Yang, W. Gilbert, F. E. Hudson, K. M. Itoh, A. A. Kiselev, T. D. Ladd, A. Morello, A. Laucht, A. S. Dzurak, Single-spin qubits in isotopically enriched silicon at low magnetic field. *Nat. Commun.* **10**, 5500 (2019).

33. C. H. Yang, W. H. Lim, F. A. Zwanenburg, A. S. Dzurak, Dynamically controlled charge sensing of a few-electron silicon quantum dot. *AIP Advances* **1**, 042111 (2011).

34. A. C. Johnson, J. R. Petta, C. M. Marcus, M. P. Hanson, A. C. Gossard, Singlet-triplet spin blockade and charge sensing in a few-electron double quantum dot. *Phys. Rev. B* **72**, 165308 (2005).

35. P. Harvey-Collard, B. D'Anjou, M. Rudolph, N. T. Jacobson, J. Dominguez, G. A. ten Eyck, J. R. Wendt, T. Pluym, M. P. Lilly, W. A. Coish, M. Pioro-Ladrière, M. S. Carroll, High-fidelity single-shot readout for a spin qubit via an enhanced latching mechanism. *Phys. Rev. X* **8**, 021046 (2018).

36. W. Huang, M. Veldhorst, N. M. Zimmerman, A. S. Dzurak, D. Culcer, Electrically driven spin qubit based on valley mixing. *Phys. Rev. B* **95**, 075403 (2017).

37. T. Tanttu, B. Hensen, K. W. Chan, C. H. Yang, W. W. Huang, M. Fogarty, F. Hudson, K. Itoh, D. Culcer, A. Laucht, A. Morello, A. Dzurak, Controlling spin-orbit interactions in silicon quantum dots using magnetic field direction. *Phys. Rev. X* **9**, 021028 (2019).

38. Y. Chou, H. Lu, in *2011 IEEE International Symposium on Electromagnetic Compatibility* (IEEE, 2011), pp. 6–10.

39. CST Microwave Studio, 3DS Dassault Systemes.

40. P. W. Chapman, O. N. Tufte, J. D. Zook, D. Long, Electrical properties of heavily doped silicon. *J. Appl. Phys.* **34**, 3291–3295 (1963).